Journal of Materials Chemistry A

ROYAL SOCIETY OF CHEMISTRY

PAPER

View Article Online
View Journal | View Issue

Cite this: J. Mater. Chem. A, 2023, 11, 15792

High ionic conducting rare-earth silicate electrolytes for sodium metal batteries†

Abinaya Sivakumaran,[a] Alfred Junio Samson,[a] Afshana Afroj Bristi,[a] Vishnu Surendran,[a] Shantel Butler,[b] Samuel Reid[b] and Venkataraman Thangadurai *[a]

Solid-state sodium-ion batteries (SIBs) are a viable alternative to existing lithium-ion batteries (LIBs) due to the low cost and abundance of sodium and the high safety of using solid-state components. Here, we report novel composite sodium silicate electrolytes exhibiting high ionic conductivity for solid-state SIBs. Rare-earth silicates $(3 + x)Na_2O–Gd_2O_3–6SiO_2$ (NGS, x = 0, 0.05, 0.1, 0.15, 0.2, and 0.25 mol%, following the composition $Na_3GdSi_3O_9$), are prepared by the conventional solid-state method. The phase and morphology of the prepared ceramic electrolytes are characterized using powder X-ray diffraction and scanning electron microscopy. The electrical properties of the samples are investigated using impedance spectroscopy, with NGS 0.15 mol% Na_2O, (3.45 $Na_2O–Gd_2O_3–6$ SiO_2; NGS15) sintered at 1075 °C for 6 h exhibiting the highest ionic conductivity of 7.25×10^{-4} S cm^{-1} at 25 °C comparable to that of NASICON electrolytes. Na plating/stripping is conducted to demonstrate the compatibility of the prepared ceramic electrolyte with a sodium metal anode that exhibits exceptional stability for 1000 h at a current density of 0.1 mA cm^{-2}. A hybrid battery built using a Na anode, an NGS15 ceramic electrolyte with 20 μL of liquid electrolyte on the cathode side, and a $Na_3V_2(PO_4)_3$ cathode exhibited an initial discharge capacity of 90 mA h g^{-1} at 0.1C with a capacity retention of 98.01% for 100 charge–discharge cycles, highlighting the potential of the sodium rare-earth silicate as a sodium battery separator and electrolyte.

Received 8th April 2023
Accepted 20th June 2023

DOI: 10.1039/d3ta02128a

rsc.li/materials-a

10th anniversary

Journal of Materials Chemistry (JMC) A has provided us with an avenue to showcase our research findings in solid electrolytes and electrodes for electrocatalysis, solid-oxide fuel cells, and solid-state batteries. Our original reviews and research articles published in this journal have garnered some of the highest citations among our publications. This visibility is a testament to the expanding readership of JMC A and the growing interest in materials chemistry for energy and sustainability applications. The journal is a source of high-quality original articles for us, and we commend the editorial and advisory board experts for the rigorous and efficient peer review.

1. Introduction

Lithium-ion batteries (LIBs) are the energy storage of choice for electric cars, portable gadgets, sensors, and touch displays. LIBs offer high energy density, minimal maintenance, low self-discharge, and reliability.[1–3] However, supply and production risks in LIB raw materials such as lithium, nickel, and especially cobalt are already being predicted by scientists.[4,5] Sodium-ion batteries (SIBs) are a promising replacement for LIBs due to their abundance, low cost, and the geographically widespread availability of sodium. Moreover, SIBs also operate *via* the "rocking chair" mechanism of intercalation and deintercalation.[6,7] Potassium-ion batteries (PIBs) are also gaining more interest while selecting cathode materials for PIBs is crucial.[8] Other energy storage technologies like supercapacitors are of great interest for flexible electronics. However, the major drawback is the low energy density compared to commercial LIBs.[9–11] Conventional batteries primarily rely on organic liquid electrolytes for high ionic conductivity and good electrode wettability; however, flammability and dendrite formation upon continuous charge/discharge cycles pose severe safety concerns such as fire and explosions and limit metal anode utilization.[12] Solid electrolytes are an excellent alternative to liquid electrolytes as they enhance safety by eliminating flammability, suppressing dendrite formation and providing superior thermal stability.[13–15]

Na-β-alumina is a widely used solid electrolyte in commercial sodium–sulfur batteries, which operate mainly at high temperatures, 300 °C.[16,17] However, this restricts its

[a]Department of Chemistry, University of Calgary, 2500 University Dr NW, Calgary, Alberta, T2N 1N4, Canada. E-mail: vthangad@ucalgary.ca

[b]Geometric Energy Corporation, 1400–3507 Ave SW, Calgary, Alberta, T2P 3N9, Canada

† Electronic supplementary information (ESI) available. See DOI: https://doi.org/10.1039/d3ta02128a

applications, compelling researchers to explore electrolyte alternatives that operate at lower temperatures. Among the various solid-state electrolytes for sodium-ion batteries, a class of compounds with the composition $Na_3Zr_2Si_2PO_{12}$, introduced as "sodium superionic conductor" (NASICON) ceramics by John Goodenough and co-workers in 1976, attracted the most attention due to its excellent room-temperature (RT) ionic conduction.[18] $Na_3Zr_2Si_2PO_{12}$ has an ionic conductivity of 10^{-3} S cm^{-1} at RT, good electrochemical and thermal stability, and a three-dimensional network structure that allows facile ionic movement. Recent research has shown that the conductivity of NASICON-type solid electrolytes can be further improved through elemental doping.[19,20]

Polymer-based solid electrolytes are another type of inorganic solid electrolytes; they are thin, flexible, and easily synthesized by solution casting.[21–23] Even though polymers exhibit lower RT ionic conductivity ($\sim 10^{-5}$ S cm^{-1}) compared to other inorganic solid electrolytes ($\sim 10^{-4}$ S cm^{-1}), they have good interfacial contact with electrodes. In order to obtain the benefits of both ceramics and polymer, composite electrolytes with high ionic conductivity and low interfacial resistance to electrodes have been developed.[24–26] Sulfides are another class of inorganic solid electrolytes with high RT ionic conductivity (10^{-3} S cm^{-1}).[27–29] However, these materials are unstable with the metal anode and the ambient atmosphere and exhibit narrow electrochemical stability windows.[30,31]

Rare-earth silicates, $Na_xMSi_yO_z$ (M = rare-earth elements), are materials discovered in the 1970s.[32,33] $Na_xMSi_yO_z$ is generally synthesized using high-temperature melt-quenching and conventional solid-state methods.[34] However, other synthesis techniques were reported, including freeze-drying, hydrothermal, and sol–gel.[33,35,36] Silicate materials have a similar structure to that of NASICON with MO_6 octahedra and SiO_4 tetrahedra. In the structure, SiO_4 tetrahedra are linked to form puckered $Si_{12}O_{36}$ rings parallel to the basal plane of the hexagonal cell, providing path for facile ionic movement.[33,37] These materials also have the advantage of low sintering temperature ($\sim$1500 °C) comparing Na-β-alumina (>1600 °C).[38] The ionic conductivity was found to be lower, even at higher temperatures. Despite moderate ionic conductivity, obtaining a single phase of silicates has been a significant concern since its discovery. Several techniques were carried out to obtain phase pure silicates by modifying the synthesis routes, architecture, and sintering temperatures, thus achieving an ionic conductivity in the range of 10^{-3} S cm^{-1} at RT.[36,39–41] The application of these silicates as a solid electrolyte is rarely explored.

In this study, we have revisited the less-studied rare-earth silicate composition, $Na_3GdSi_3O_9$, and attempted to synthesize using the conventional solid-state method. We have expressed the composition as a mixture of oxides $(3 + x)Na_2O$–Gd_2O_3–$6SiO_2$ ($x = 0$, 0.05, 0.1, 0.15, 0.2, and 0.25 mol%) with varying Na excess that compensates for Na volatile losses during high-temperature sintering. Two solid state synthesis routes were employed to obtain a phase pure $Na_3GdSi_3O_9$. The study highlights the challenge of obtaining a single-phase material. Despite the multiple phases present in the composition, we have found that the oxides exhibit ionic conductivities reaching approximately 10^{-3} S cm^{-1} at 25 °C. Further studies could optimize the material composition, providing prospects for silicates in solid-state Na batteries.

2. Experimental section

2.1 Solid electrolyte synthesis

Na_2O–Gd_2O_3–SiO_2 (NGS) ceramic electrolytes were prepared by a conventional solid-state approach using $NaNO_3$ (98%, Alfa Aesar), Gd_2O_3 (99.9%, Alfa Aesar), and SiO_2 (99%, Alfa Aesar) as the precursor materials. The targeted stoichiometric composition was $Na_3GdSi_3O_9$. Compounds with 0, 5, 10, 15, 20, and 25% Na excess corresponds to the mixtures $3Na_2O$–Gd_2O_3–$6SiO_2$ (NGS-0), $3.15Na_2O$–Gd_2O_3–$6SiO_2$ (NGS-5), $3.3Na_2O$–Gd_2O_3–$6SiO_2$ (NGS-10), $3.45Na_2O$–Gd_2O_3–$6SiO_2$ (NGS-15), $3.6Na_2O$–Gd_2O_3–$6SiO_2$ (NGS-20), and $3.75Na_2O$–Gd_2O_3–$6SiO_2$ (NGS-25), respectively. Two synthesis routes were carried out to obtain the targeted phase. In route 1, stoichiometric amounts of the precursors were mixed in a high-energy ball mill (Pulverisette, Fritsch, Germany) for 6 h at 200 rpm with isopropanol as the solvent. The dried powders were then calcined at 900 °C for 6 h to decompose the nitrates and carbonates. After ball milling, the resultant powder was pressed into pellets by isostatic pressing before final sintering at the desired temperature for 6 h at a heating rate of 5 °C min^{-1}.

Route 2 follows the initial mixing and calcining procedures in route 1. However, after calcining at 900 °C and ball milling for 6 h, the whole batch was pressed into rods and sintered at desired temperatures for 6 h. The rods were then crushed and ball-milled for 12 h at 200 rpm. This intermediate step should allow further mixing and reaction between precursors. Fig. S1a and b† report the steps used in routes 1 and 2, respectively (see ESI†).

2.2 Materials characterization

Powder X-ray diffraction (PXRD) with a Bruker D8 powder X-ray Advance diffractometer and Cu-Kα radiation (40 kV; 40 mA) was employed for phase analysis of the compounds. In addition, morphological analysis was done using scanning electron microscopy (SEM) (Zeiss Sigma VP Field Emission SEM).

2.3 Electrochemical characterization

Electrochemical performances were conducted using a Solartron SI 1260 impedance and gain-phase analyzer (0.1 Hz to 1 MHz; 100 mV). Au current collectors were painted on both sides of the prepared ceramic pellets and fired at 700 °C for 1 h to ensure a good interface. The Na|NGS15|Na symmetric cells were assembled using CR2032 coin cells inside an argon-filled glovebox to study the interfacial stability between the Na metal anode and NGS15 solid electrolyte. We conducted a systematic study to determine the best liquid electrolyte compatible with the silicate solid electrolyte for the hybrid battery.

Four liquid electrolytes were prepared using two different sodium salts, sodium perchlorate (NaClO4) and sodium hexafluorophosphate (NaPF6) and three different solvents such as propylene carbonate (PC), ethylene carbonate (EC) and

fluoroethylene carbonate (FEC). These electrolyte compositions are named as, 1 M $NaClO_4$ in PC : FEC (95 : 05 wt%), 1 M $NaClO_4$ in EC : PC (50 : 50 wt%), 1 M $NaPF_6$ in PC : FEC (95 : 05 wt%) and 1 M $NaPF_6$ in EC : PC (50 : 50 wt%). We compared sodium metal batteries with liquid electrolytes using a Na anode, a 40 μL prepared liquid electrolyte on both sides of the separator (Whatman glass microfiber) and an in-house synthesized NVP cathode. The NVP cathode was prepared by forming a slurry of NVP powder, super P conductive carbon and polyvinylidene fluoride (PVDF) binder in an 8 : 1 : 1 ratio. The NVP was synthesized following the procedure outlined in our previous study.[42] The slurry was then coated onto an aluminium current collector using a doctor blade and vacuum-dried overnight at 60 °C. Finally, circular disks with a 1 cm diameter were cut from the coated material. The average active material loading was 1.38 mg cm^{-2}.

Similarly, hybrid batteries were fabricated using Na anode, NGS15 ceramic electrolyte, 20 μL of the above-prepared liquid electrolytes and NVP cathode. Adding twenty microliters of the respective liquid electrolyte on the cathode side reduces the interfacial resistance. In addition, these hybrid batteries were also tested to evaluate the feasibility of the ceramic as a separator in sodium-ion batteries.

3. Results and discussion

3.1 XRD

The PXRD data obtained for NGS ceramics sintered at 1050 °C for 6 h utilizing route 1 (using $NaNO_3$, Gd_2O_3, and SiO_2 precursors) along with the possible matching reference patterns are shown in Fig. 1. The reference patterns include $Na_3GdSi_3O_9$ (powder diffraction file (PDF) no. 00-035-0142), $Na_5GdSi_4O_{12}$ (rhombohedral; PDF: 00-035-0141), $Na_9GdSi_6O_{18}$ (hexagonal; PDF 00-056-0122), $Na_3GdSi_2O_7$ (PDF: 00-056-0185), $NaGdSiO_4$ (orthorhombic; PDF: 00-035-0013), and $NaGdSiO_4$ (tetragonal; PDF: 00-035-0012). The XRD diffractograms of NGS 0 and 25 samples are broadened, suggesting amorphous nature, while others demonstrate crystalline behaviour with distinct high intense peaks. The diffractogram of NGS 5 to 20 is multi-phased, with the significant phase being $Na_5GdSi_4O_{12}$.

Multiple ball milling and sintering enhance component mixing and reactivity, removing impurity phases.[33] Thus, we adopted two ball milling and sintering steps in route 2. Fig. S2a† shows the XRD pattern of ceramics prepared through route 2. The compositions NGS0 and 25 were not studied further since they exhibit low ionic conductivity. NGS5, 10, and 20 were also multi-phased, with the major phase being $Na_5GdSi_4O_{12}$ as in route 1 (see ESI†) while, NGS15 consists mainly of $Na_3GdSi_3O_9$ (PDF: 00-035-0142) with no impure phases. We made numerous batches of NGS15 to study the reproducibility of the procedure. However, we could not obtain an almost phase-pure sample, as shown in Fig. S2a.† This agrees with the difficulties in achieving pure phase silicates by conventional synthesis.[33,36,43]

Different sintering temperatures (950, 1000, 1050, and 1075 °C) and various precursors (Na_2CO_3, Gd $(NO_3)_3$, and $Si(OCOCH_3)_4$) were also tried in route 1 to improve the purity of the phase. However, the resulting phases were still multi-phase

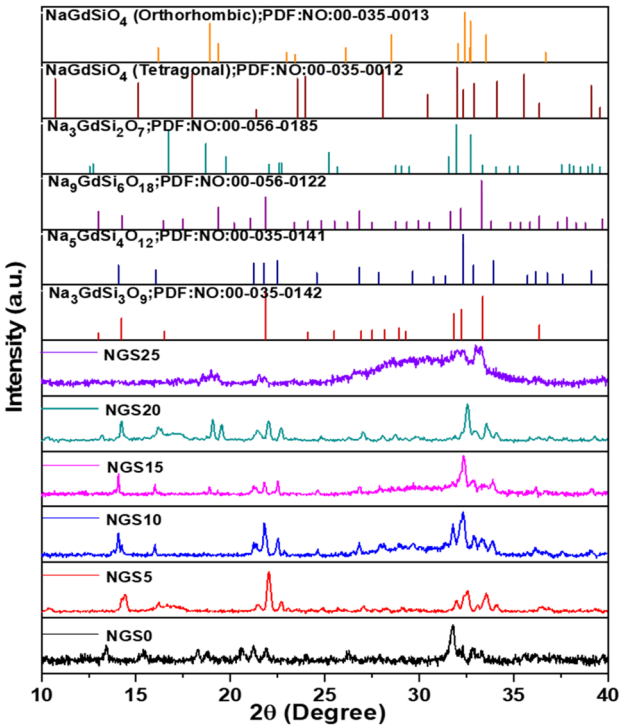

Fig. 1 PXRD patterns of NGS0-NGS25 prepared by route 1 along with the reference patterns of $Na_3GdSi_3O_9$ (PDF: 00-035-0142), $Na_5GdSi_4O_{12}$ (PDF: 00-035-0141) (rhombohedral), $Na_9GdSi_6O_{18}$ (PDF 00-056-0122), $Na_3GdSi_2O_7$ (PDF: 00-056-0185) (hexagonal), $NaGdSiO_4$ (orthorhombic phase; PDF: 00-035-0013), and $NaGdSiO_4$ (tetragonal phase; PDF: 00-035-0012).

along with some unknown phases, as in Fig. S2b and c (see ESI†). Hence, the investigated compounds in this study are considered composite materials consisting of various sodium silicates comprising Na_2O–Gd_2O_3–SiO_2. Phase diagram of selected composition with prepared six NGS compositions from NGS0–NGS25 is marked based on mol% in Fig. S3.†

3.2 Morphology

SEM analysis was performed on the NGS ceramics prepared by routes 1 and 2 to investigate their morphologies. The cross-sectional SEM micrographs of NGS5–20 are shown in Fig. 2a–d for route 1 and in Fig. 2e–h for route 2, respectively. All the samples exhibit irregular densified surfaces with some voids. No noticeable difference in morphology was observed for samples prepared by routes 1 and 2. In route 1, NGS15 has a minimum number of pores and appears the densest, which helps reduce grain boundary resistance. In route 2, NGS15 and 20 seem to be denser than others.

3.3 Electrochemical performance

Impedance spectroscopy was used to determine the electrical properties of the prepared sodium gadolinium silicates. The conductivity, σ, is calculated using the eqn (1):

$$\sigma = \left(\frac{1}{R}\right)\left(\frac{l}{a}\right) \quad (1)$$

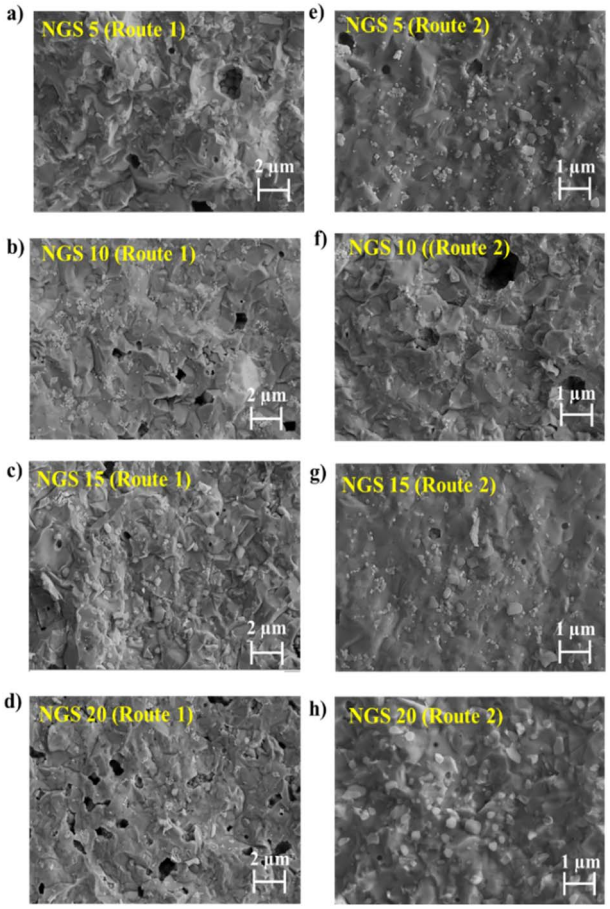

Fig. 2 SEM images of the cross-section of NGS5-20 pellets (a)–(d) route 1 and (e)–(h) route 2, respectively.

where R is the resistance at the low-frequency intercept before the Na blocking tail, l is the thickness, and a is the area of the electrolyte. The activation energies, E_a, of all the samples, were estimated using the Arrhenius eqn (2):

$$\sigma T = A \exp\left(\frac{-E_a}{kT}\right) \quad (2)$$

A is the pre-exponential factor, E_a is the activation energy, T is the temperature, and k is the Boltzmann constant (1.38×10^{-23} J K^{-1}).

The results from NGS0 and 25 were not included since they had high impedance (ionic conductivities between 10^{-6} to 10^{-8} S cm^{-1}) at RT. From Fig. 3a, NGS15 exhibited the lowest grain boundary resistance. The equivalent circuit is fitted to the RT impedance of NGS15, shown in the inset. The impedance data of NGS15 shows a semicircle at high frequencies and a tail at low frequencies, corresponding to the grain-boundary response and the blocking electrode response of the Au electrode/current collector, respectively.

From Fig. 3b, NGS15 and 20 had the lowest grain boundary resistance, consistent with the morphology observed in SEM. Fig. 3c and d illustrate the Arrhenius plot of the samples (25 to 150 °C) prepared by routes 1 and 2. The conductivity values of NGS5, 10, 15, and 20 are close throughout the measured temperature range for route 1 samples, while NGS5 had a lower conductivity than others for route 2. Table S1 (see ESI†) demonstrates the ionic conductivity of all the samples prepared with different sintering conditions.

Based on Table S1,† NGS15 prepared by route 1 sintered at 1075 °C showed the highest conductivity of 7.25×10^{-4} S cm^{-1}. We also used $Gd(NO_3)_3$ and $Si(OCOCH_3)_4$ precursors to test the phase formation. However, the samples were still multi-phased, as shown in Fig. S2c (see ESI†), and no significant changes in conductivity were observed. Likewise, the samples sintered at different temperatures resulted in almost similar conductivity.

Table 1 compares the conductivity of various composite solid electrolytes with present NGS15 silicate.[45–60] Most of the composite solid electrolytes' conductivity was 10^{-5} to 10^{-7} S cm^{-1} at RT and high ionic conduction was achieved mainly above 200 °C. Moreover, these composites were developed by a melt-quenching technique, which requires high temperatures (>1300 °C) to melt the precursors. However, we prepared NGS15 silicate electrolyte by solid-state approach with lower sintering temperature (1050–1075 °C) and high ionic conductivity at RT.

The ionic conductivity of our best-conducting NGS15 composition is compared with other single phase solid electrolytes used in sodium batteries. Fig. 3e presents the Arrhenius plot illustrating several solid electrolytes, including Na-β-alumina, NASICON (sodium superionic conductor), sodium sulfides, antiperovskite and polymers. Inorganic solid electrolytes, including Na-β-alumina, NASICON, and sodium sulfides, tend to have higher ion conduction properties than polymers and antiperovskite. Particularly, NASICON prepared by Ceramatec demonstrated superior ionic conductivity over the temperature range, followed by Na-β-alumina.[44] Recently, the silicate electrolyte, $Na_5YSi_4O_{12}$ trilayer scaffold, was developed by Yang *et al.*[41] *via* tape casting technique. This trilayer (porous|dense|porous) architecture gave better RT ionic conductivity. NGS15 showed excellent conductivity comparable to Na_3PSe_4 at RT. From this comparison, it is evident that NGS15 electrolyte showed higher ionic conductivity than the majority of other solid electrolytes, including glass-ceramic c-Na_3PS_4, glass Na_2S-P_2S_5, polymer PEO-$NaClO_4$ (5%-TiO_2), polymer PEO-$NaPF_6$, and antiperovskite Na_3OBr. Even though the phase is impure, NGS15 displayed excellent ion-conducting properties relative to most single-phased solid electrolytes.

3.4 Na–NGS interface and battery performance

Galvanostatic cycling studies were conducted to investigate the interfacial stability between the Na metal anode and the NGS15 ceramic electrolyte at 25 °C. Fig. S4† shows the critical current density (CCD) graph for current densities ranging from 0.1 to 0.5 mA cm^{-2}. The maximum current density that Na|NGS15|Na symmetric cell can withstand at room temperature is 0.4 mA cm^{-2} without any interface modification. However, at 0.5 mA cm^{-2}, an apparent voltage drop and short circuit occurred due

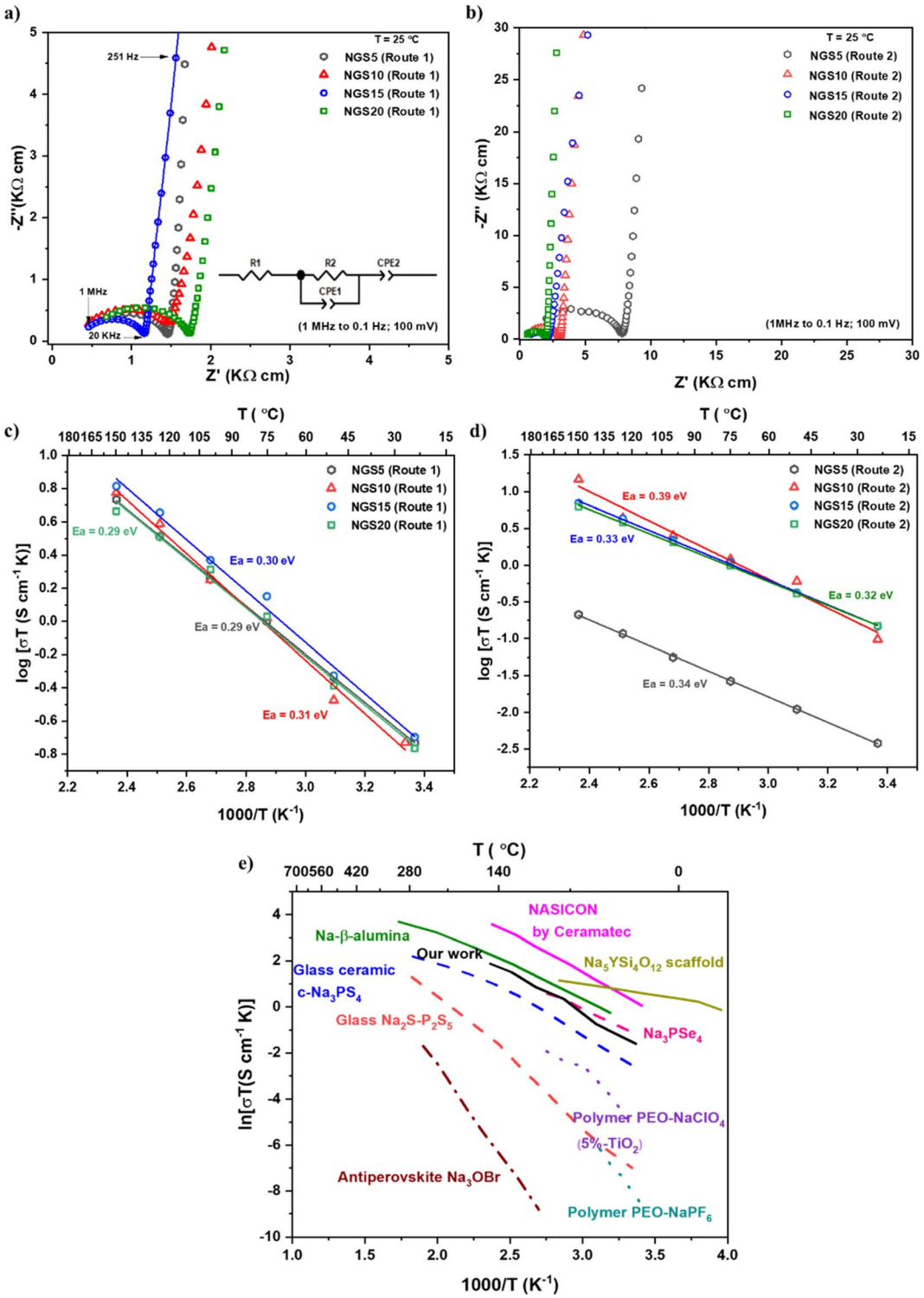

Fig. 3 (a) and (b) RT–impedance for NGS5–20 prepared *via* routes 1 and 2, respectively. (c) and (d) Arrhenius plots for NGS5–20 prepared *via* routes 1 and 2, respectively, and (e) Arrhenius plot of solid electrolytes compared with NGS15.[38,41,44]

to dendrite penetration. Fig. 4 shows the time-dependent plating/stripping profile of the Na|NGS15|Na symmetric cell at a current density of 0.1 mA cm^{-2} at 25 °C.

The polarity of the current was switched every 30 min for 1000 h. The results indicate a low overpotential of approximately 25 mV, which remained stable for 1000 cycles without any significant voltage fluctuations. This observed overpotential is due to the oxidation and reduction of Na ion transport through the electrode/electrolyte interfaces.[61] The stable galvanostatic profile further supports the mechanical

Table 1 Synthesis method and conductivity of several composite solid electrolytes along with NGS15 (conductivity at 25 °C unless specified)

No.	Composite solid electrolytes	Synthesis method	Conductivity (S cm^{-1})	Ref.
1	37.9 Na_2O–5.7 Y_2O_3–56.4 SiO_2	Melt-quenching	3×10^{-8}	45
2	Na_2Se–Ga_2Se_3–$GeSe_2$	Melt-quenching	10^{-5}	46
3	90 wt%NASICON–10 wt%60Na_2O–10Nb_2O_5–30P_2O	Melt-quenching	1.2×10^{-4}	47
4	50Na_2O–7.6SnO_2–42.4SiO_2	Melt-quenching	6×10^{-7}	48
5	Li4P_2O_7–Li_3PO_4	Solid state	3.85×10^{-5}	49
6	60Li_2O:30P_2O_5:10Nb_2O_5	Melt-quenching	2×10^{-6}	50
7	AgI–Ag_2O–P_2O_5–MoO_3	Melt-quenching	1.2×10^{-3}	51
8	$Li(BH_4)_{0.75}I_{0.25}(Li_2S)_{0.75}(P_2O_5)_{0.2}$	Solid-state	10^{-3}	52
9	0.9(0.75AgI:0.25AgCl)0.1 SiO_2	Quenching	10^{-3}	53
10	55.6 mol% Na_2O:15.3 mol/5 NbO:29.1 mol% P_2O_5	Melt-quenching	1.35×10^{-3} (300 °C)	54
11	$(Li_{0.25}–La_{0.25})_{1-x}Sr_{0.5x}NbO_3$ ($x = 0.125$)	Solid-state	7.3×10^{-5}	55
12	0.25LiCl–0.48LiO–0.03 SiO_2–0.24P_2O_5	Melt-quenching	2.5×10^{-3} (235 °C)	56
13	40 Li_2O–30.5 B_2O_3–20 SiO_2–2P_2O_5–7.5Li_2SO_4	Melt-quenching	1.5×10^{-2} (250 °C)	57
14	$LiTi_2(PO_4)_3$–0.3$Li_{2.9}B_{0.9}S_{0.1}O_{3.1}$	Solid-state	1.79×10^{-4}	58
15	LLZTO@Li4GeO_4/Li_2O	Liquid sintering	5.57×10^{-4}	59
16	2.5Li_3PS_4–0.5Li_4SnS_4	Solid-state	2.1×10^{-3} (550 °C)	60
17	NGS15 (15% Na excess–3.45Na_2O–Gd_2O_3–6SiO_2)	Solid-state	7.25×10^{-4}	This work

stability of NGS15 solid electrolyte, dendrite blocking, and good anode/electrolyte interface.

In order to evaluate the application of NGS15 solid electrolytes in energy storage systems, hybrid batteries were assembled, and their electrochemical performances were measured at RT. Adding a liquid electrolyte on the cathode side for a hybrid battery reduces interfacial resistance and improves wettability. The battery made using 1 M $NaPF_6$ in EC:PC and 1 M $NaPF_6$ in PC:FEC showed higher capacity decay, which indicates the incompatibility of $NaPF_6$-based organic liquid electrolyte with silicate solid electrolyte where the electrochemical performance is not included. The galvanostatic charge–discharge profile of hybrid batteries made using the remaining two liquid electrolytes, including 1 M $NaClO_4$ in EC:PC (50 : 50 wt%) and 1 M $NaClO_4$ in PC:FEC (95 : 5 wt%) are given in Fig. 5a and b, respectively.

The charge plateau is mainly due to the oxidation of $Na_3V_2^{(III)}(PO_4)_3$ to $NaV_2^{(IV)}(PO_4)_3$ and discharge plateau corresponds to the reduction process of $NaV_2^{(IV)}(PO_4)_3$ to $Na_3V_2^{(III)}(PO_4)_3$.

$$Na_3V_2(PO_4)_3 \leftrightharpoons 2Na^+ + 2e^- + NaV_2(PO_4)_3 \quad (3)$$

In Fig. 5b, the cell made using 1 M $NaClO_4$ in PC:FEC showed a discharge capacity of 90 mA h g^{-1} with negligible capacity decay after 10 cycles in comparison to the cell using 1M NaClO4 in EC:PC (Fig. 5a). According to literatures, 1 M $NaClO_4$-based

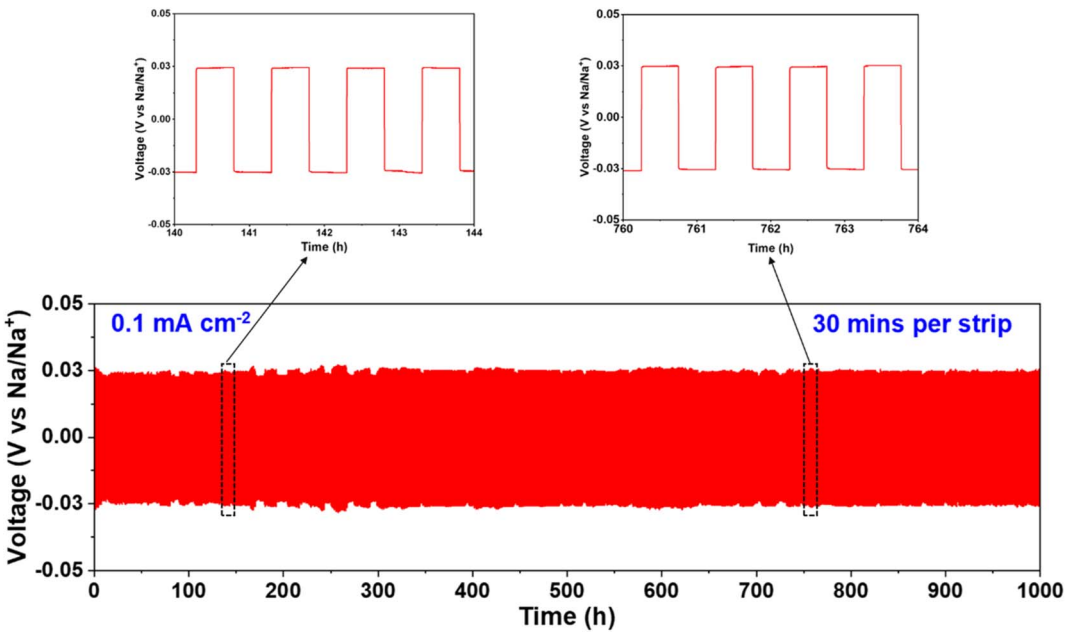

Fig. 4 Long-term stability of galvanostatic cycling at 0.1 mA cm^{-2} at 25 °C for 1000 h using Na|NGS15|Na symmetric cell.

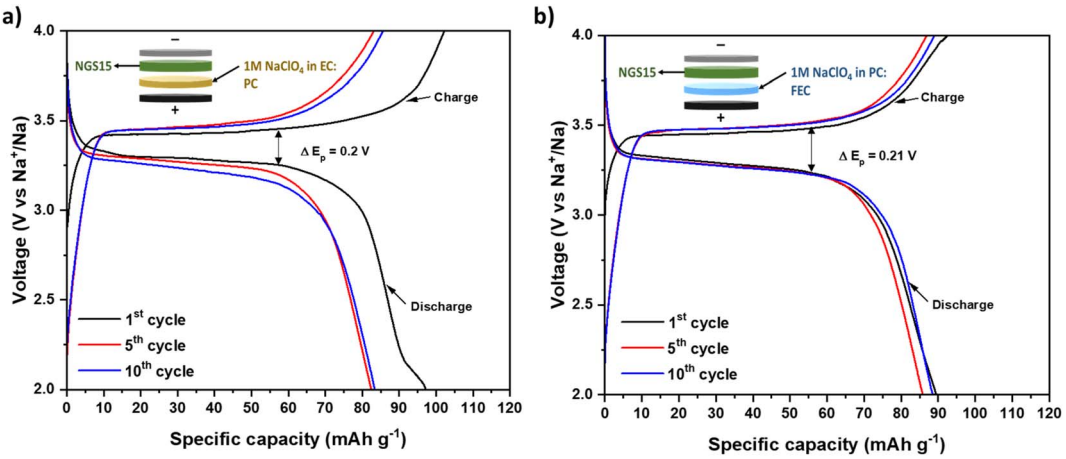

Fig. 5 Galvanostatic charge–discharge curves at 0.1C at 25 °C. (a) Na|NGS15|20 μL of 1 M $NaClO_4$ in EC:PC|NVP and (b) Na|NGS15|20 μL of 1 M $NaClO_4$ in PC:FEC|NVP (NGS15 was prepared *via* route 1).

liquid electrolyte is used widely for hybrid batteries made with NASICON solid electrolyte, consistent with our studies.[40,62–64] PC:FEC-based solvent showed better electrochemical performance than EC:PC-based solvent. This might be due to the addition of FEC additive (5 wt%), consumed during the cycling process and helps achieve a stable electrode/electrolyte interface.[65–67] To optimize the amount of liquid electrolyte needed to improve the interface for the hybrid battery, we made three more cells with different amounts (5, 10, and 15 μL) of 1 M $NaClO_4$ in PC:FEC on the cathode side. The cells made with 5 and 10 μL of liquid electrolytes got short-circuited after 1st cycle, indicating insufficient wettability and poor interface. In Fig. S5,† the cell with 15 μL of liquid electrolyte showed a high discharge capacity of 95 mA h g^{-1} in 1st cycle at 0.1C, but the

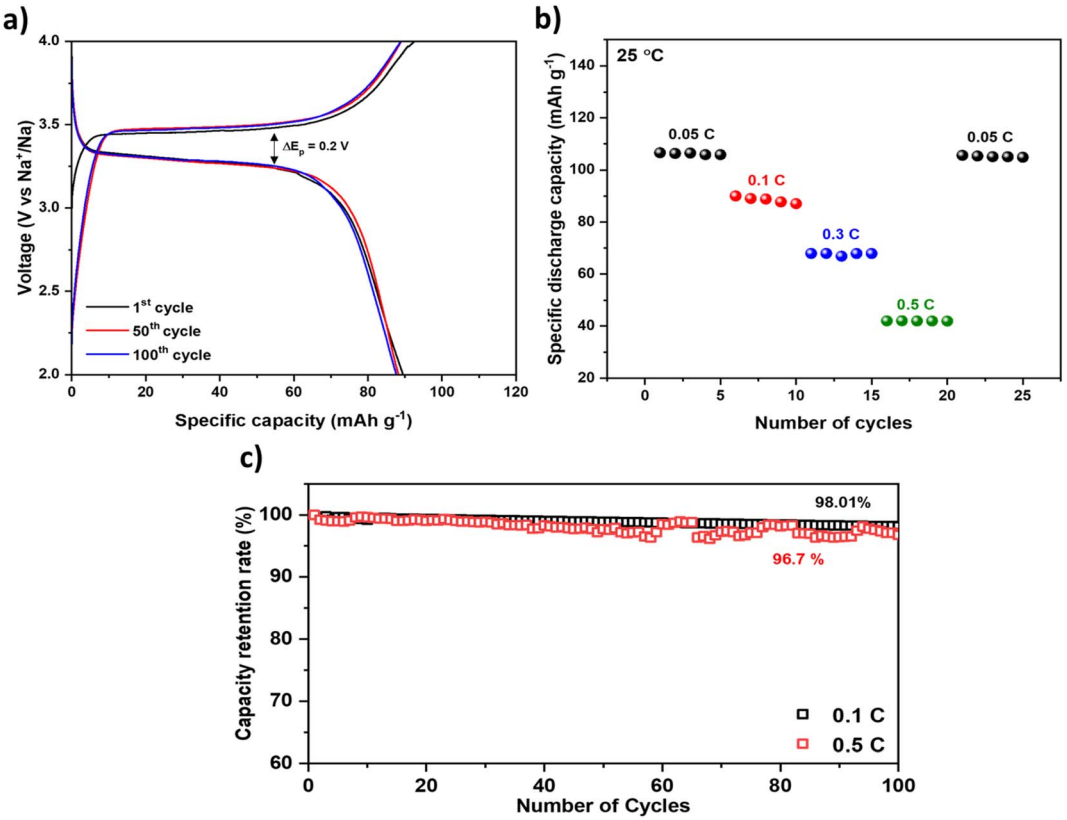

Fig. 6 (a) Galvanostatic charge–discharge curves of 1st, 50th and 100th cycles of Na|NGS15|20 μL of 1 M $NaClO_4$ in PC:FEC|NVP hybrid battery at 0.1C at 25 °C. (b) Rate performance at different C rates, (c) Capacity retention at 0.1 and 0.5C for 100 cycles (NGS15 was prepared *via* route 1).

capacity decay is higher than the cell with 20 μL of liquid electrolyte. Therefore, we optimized that 20 μL of liquid electrolyte is sufficient to improve the wettability and form a stable electrode/electrolyte interface, thus providing excellent electrochemical performance. The charge–discharge profiles of batteries made using only liquid electrolytes at 0.1C (25 °C) are given in Fig. S6† for comparison.

From the battery performances, 1 M $NaPF_6$ in PC:FEC showed a higher discharge capacity of 110 mA h g^{-1} (close to the theoretical capacity of NVP) with low-capacity decay and overpotential at 0.1C. Fig. 6a displays the 1st, 50th, and 100th charge–discharge curves of the best hybrid battery using PC:FEC based electrolytes at 0.1C at 25 °C. There is less capacity degradation from the 1^{st} to 100^{th} cycle. The rate performance of the hybrid battery for 5 cycles from 0.05C to 0.5C is displayed in Fig. 6b, where the capacity at 0.05C is maintained, which shows the reversibility of the hybrid battery performance. The inferior specific capacity at a higher C rate (0.5C) is attributed to the low electronic conductivity of the NVP cathode material.[42] Fig. 6c shows the cycling performance at 0.1 and 0.5C rates for 100 cycles. At 0.1C, the system is stable for 100 cycles without significant capacity decay, achieving 98.01% capacity retention. In contrast, there is a degradation and fluctuations in the specific discharge capacity at 0.5C. Despite capacity fluctuations, the cell demonstrated a remarkable capacity retention of 96.7% after 100 cycles at a rate of 0.5C.

To investigate whether capacity decay is associated with the structural stability of the NGS15 solid electrolyte, we performed the X-ray diffraction (XRD) analysis after cycling. The XRD data before and after cycling is compared in Fig. S7.† According to the graph, no phase change was observed, with all the peaks matching, demonstrating the excellent stability of the solid electrolyte. The capacity decay can be attributed to other contributing factors, including the structural degradation of the cathode, the formation of a solid-electrolyte interphase (SEI) layer on the cathode surface, side reactions with the electrolyte, and the dissolution of active species into the electrolyte.[68–71] Additionally, the volume changes experienced by the NVP cathode during the deintercalation of Na ions can result in lattice stress, leading to cracking and detachment of the particle. This structural instability contributes to capacity decay and the occurrence of side reactions.[72–74] We further evaluated the long-term stability at 0.5C for 500 cycles, as shown in Fig. S8.† Remarkably, even after 500 charge–discharge cycles, the cell retained 90.8% of its initial capacity. These electrochemical studies prove silicates can be a potential candidate as solid electrolyte for sodium batteries.

4. Conclusions

In summary, we aimed to synthesize $Na_3GdSi_3O_9$ ceramic electrolyte *via* a conventional solid-state approach. The composition was expressed as $(3 + x)Na_2O–Gd_2O_3–6SiO_2$ ($x = 0.05$, 0.1, 0.15, 0.2 and 0.25 mol%), and excess $NaNO_3$ was added to compensate for the Na loss during high-temperature sintering. In addition, the effect of varying synthesis routes, excess Na, and sintering temperature was investigated. The obtained ceramic materials consisted of multiple phases of several rare-earth silicate compositions. The optimized ceramic with 0.15 mol% excess Na_2O, NGS15 ($0.35Na_2O–Gd_2O_3–6SiO_2$), sintered at 1075 °C for 6 h *via* route 1 exhibited the highest conductivity of 7.25×10^{-4} S cm^{-1} at 25 °C. Na|NGS15|Na symmetric cell showed good interfacial stability between Na anode and NGS15 ceramic electrolyte over 1000 h at 0.1 mA cm^{-2}. Furthermore, the assembled hybrid battery Na|NGS15|20 μL of 1 M $NaClO_4$ in PC:FEC|NVP exhibited a discharge capacity of 90 mA h g^{-1} at 0.1C with 98.01% capacity retention for 100 charge–discharge cycles. Thus, $Na_2O–Gd_2O_3–SiO_2$ composite ceramics are excellent solid electrolyte for solid-state SIBs, paving the way for more sustainable, cost-effective, and safe electrolytes for sodium batteries.

Author contributions

Methodology, experimental work, data collection, investigation and analysis, validation, writing – original draft, review and editing – Abinaya Sivakumaran; methodology, investigation and analysis, validation, draft review and editing – Alfred Samson; draft review and editing – Afshana Afroj Bristi; investigation, draft review and editing – Vishnu Surendran; supervision, conceptualization, draft review and editing, project administration and funding, communications – Venkataraman Thangadurai; draft review, discussion, and editing – Shantel Butler; draft review and editing and funding – Samuel Reid.

Conflicts of interest

There are no conflicts of interest to declare.

Acknowledgements

This work was funded by the Natural Sciences and Engineering Research Council of Canada (NSERC) Collaborative Research and Development (CRD) Grants and Geometric Energy Corporation, Calgary.

Notes and references

1 J. B. Goodenough and K. S. Park, *J. Am. Chem. Soc.*, 2013, **135**, 1167–1176.
2 J. B. Goodenough and Y. Kim, *Chem. Mater.*, 2010, **22**, 587–603.
3 J. B. Goodenough and Y. Kim, *J. Power Sources*, 2011, **196**, 6688–6694.
4 C. Vaalma, D. Buchholz, M. Weil and S. Passerini, *Nat. Rev. Mater.*, 2018, **3**, 18013.
5 E. A. Olivetti, G. Ceder, G. G. Gaustad and X. Fu, *Joule*, 2017, **1**, 229–243.
6 C. Delmas, *Adv. Energy Mater.*, 2018, **8**, 1703137.
7 M. D. Slater, D. Kim, E. Lee and C. S. Johnson, *Adv. Funct. Mater.*, 2013, **23**, 947–958.
8 S. Liu, L. Kang and S. C. Jun, *Adv. Mater.*, 2021, **33**, 2004689.
9 S. Liu, L. Kang, J. Zhang, S. C. Jun and Y. Yamauchi, *NPG Asia Mater.*, 2023, **15**, 9.

10 S. Liu, L. Kang, J. Zhang, E. Jung, S. Lee and S. C. Jun, *Energy Storage Mater.*, 2020, **32**, 167–177.
11 S. Liu, L. Kang, J. Hu, E. Jung, J. Zhang, S. C. Jun and Y. Yamauchi, *ACS Energy Lett.*, 2021, **6**, 3011–3019.
12 V. Thangadurai and B. Chen, *Chem. Mater.*, 2022, **34**, 6637–6658.
13 W. Zhou, Y. Li, S. Xin and J. B. Goodenough, *ACS Cent. Sci.*, 2017, **3**, 52–57.
14 C. Zhou, S. Bag and V. Thangadurai, *ACS Energy Lett.*, 2018, **3**, 2181–2198.
15 C. Sun, J. Liu, Y. Gong, D. P. Wilkinson and J. Zhang, *Nano Energy*, 2017, **33**, 363–386.
16 R. M. Dell and P. T. Moseley, *J. Power Sources*, 1981, **6**, 143–160.
17 A. Hooper, *J. Phys. D: Appl. Phys.*, 1977, **10**, 1487–1496.
18 J. B. Goodenough, H.-P. Hong and J. A. Kafalas, *Mater. Res. Bull.*, 1976, **11**, 203–220.
19 Y. Lu, J. A. Alonso, Q. Yi, L. Lu, Z. L. Wang and C. Sun, *Adv. Energy Mater.*, 2019, 9.
20 L. Lu, Y. Lu, J. A. Alonso, C. A. López, M. T. Fernández-Díaz, B. Zou and C. Sun, *ACS Appl. Mater. Interfaces*, 2021, **13**, 42927–42934.
21 H. Zhang and M. Armand, *Isr. J. Chem.*, 2021, **61**, 94–100.
22 A. Murali, M. Sakar, S. Priya, V. Vijayavarman, S. Pandey, R. Sai, Y. Katayama, M. Abdul Kader and K. Ramanujam, *Mater. Lett.*, 2022, **313**, 131764.
23 A. A. Bristi, A. J. Samson, A. Sivakumaran, S. Butler and V. Thangadurai, *ACS Appl. Energy Mater.*, 2022, **5**, 8812–8822.
24 B. P. Dubey, A. Vinodhkumar, A. Sahoo, V. Thangadurai and Y. Sharma, *ACS Appl. Energy Mater.*, 2021, **4**, 5475–5485.
25 Y. Liu, B. Xu, W. Zhang, L. Li, Y. Lin and C. Nan, *Small*, 2020, **16**, 1902813.
26 L. Lu, C. Sun, J. Hao, Z. Wang, S. F. Mayer, M. T. Fernández-Díaz, J. A. Alonso and B. Zou, *Energy Environ. Mater.*, 2022, 12364.
27 A. Hayashi, A. Sakuda and M. Tatsumisago, *Front. Energy Res.*, 2016, **4**, 1–6.
28 M. Tatsumisago and A. Hayashi, *Int. J. Appl. Glass Sci.*, 2014, **5**, 226–235.
29 K. H. Park, Q. Bai, D. H. Kim, D. Y. Oh, Y. Zhu, Y. Mo and Y. S. Jung, *Adv. Energy Mater.*, 2018, **8**, 1800035.
30 L. M. Riegger, S.-K. Otto, M. Sadowski, S. Jovanovic, O. Kötz, S. Harm, L. G. Balzat, S. Merz, S. Burkhardt, F. H. Richter, J. Sann, R.-A. Eichel, B. V. Lotsch, J. Granwehr, K. Albe and J. Janek, *Chem. Mater.*, 2022, **34**, 3659–3669.
31 A. Hayashi, K. Noi, A. Sakuda and M. Tatsumisago, *Nat. Commun.*, 2012, **3**, 2–6.
32 B. A. Maksimov and Y. A. Kharitonov, *Sov. Phys. Dokl.*, 1973, **18**, 1072–1075.
33 R. D. Shannon, B. E. Taylor, T. E. Gier, H. Y. Chen and T. Berzins, *Inorg. Chem.*, 1978, **17**, 958–964.
34 S. Narayanan, S. Butler, S. Reid, and V. Thangadurai, *US Pat.*, US2022/0271330A1, 2022.
35 K. Yamashita and P. Nicholson, *Solid State Ionics*, 1985, **17**, 115–120.
36 J. J. Bentzen and P. S. Nicholson, *Mater. Res. Bull.*, 1980, **15**, 1737–1745.
37 R. D. Shannon, H.-Y. Chen and T. Berzins, *Mater. Res. Bull.*, 1977, **12**, 969–973.
38 A. Sivakumaran, A. J. Samson and V. Thangadurai, *Energy Technol.*, 2023, 2201323.
39 N. Fakhar-Bourguiba, N. Gharbi, L. Smiri-Dogguy and J. P. Boilot, *Mater. Res. Bull.*, 1988, **23**, 1185–1191.
40 G. Sun, X. Yang, N. Chen, S. Yao, X. Wang, X. Jin, G. Chen, Y. Xie and F. Du, *Energy Storage Mater.*, 2021, **41**, 196–202.
41 A. Yang, R. Ye, H. Song, Q. Lu, X. Wang, E. Dashjav, K. Yao, D. Grüner, Q. Ma, F. Tietz and O. Guillon, *Carbon Energy*, 2023, e371.
42 S. Bag, H. Murarka, C. Zhou, A. Bhattacharya, D. Jokhakar, V. G. Pol and V. Thangadurai, *ACS Appl. Energy Mater.*, 2020, **3**, 8475–8486.
43 S. Shalini, P. Sandhyarani, Y. S. Rao, D. Chakravarty and R. Subasri, *Ceram. Int.*, 2012, **38**, 295–300.
44 K. Vignarooban, R. Kushagra, A. Elango, P. Badami, B.-E. Mellander, X. Xu, T. G. Tucker, C. Nam and A. M. Kannan, *Int. J. Hydrogen Energy*, 2016, **41**, 2829–2846.
45 M. Alexander and B. Riley, *Solid State Ionics*, 1986, **18–19**, 478–482.
46 S. K. Kim, A. Mao, S. Sen and S. Kim, *Chem. Mater.*, 2014, **26**, 5695–5699.
47 T. Honma, M. Okamoto, T. Togashi, N. Ito, K. Shinozaki and T. Komatsu, *Solid State Ionics*, 2015, **269**, 19–23.
48 I. S. Kovyazina, G. V. Nechaev, S. G. Vlasova and O. G. Reznitskikh, *Glass Phys. Chem.*, 2017, **43**, 146–150.
49 E. Kartini, V. Yapriadi, H. Jodi, M. Manawan, C. Panghegar and Wahyudianingsih, *Prog. Nat. Sci.: Mater. Int.*, 2020, **30**, 168–173.
50 T. Okada, T. Honma and T. Komatsu, *Mater. Res. Bull.*, 2010, **45**, 1443–1448.
51 K. Singh, G. Chiodelli and A. Magistris, *J. Power Sources*, 1996, **58**, 103–106.
52 A. El kharbachi, Y. Hu, K. Yoshida, P. Vajeeston, S. Kim, M. H. Sørby, S. Orimo, H. Fjellvåg and B. C. Hauback, *Electrochim. Acta*, 2018, **278**, 332–339.
53 R. C. Agrawal, M. L. Verma and R. K. Gupta, *J. Phys. D: Appl. Phys.*, 1998, **31**, 2854–2860.
54 S. Barth and A. Feltz, *Solid State Ionics*, 1989, **34**, 41–45.
55 Y. Kawakami, M. Fukuda, H. Ikuta and M. Wakihara, *Solid State Ionics*, 1998, **110**, 187–192.
56 P. Tsai and M. Greenblatt, *J. Non-Cryst. Solids*, 1988, **103**, 101–107.
57 M. A. Salorkar, K. Gour and V. K. Deshpande, *J. Alloys Compd.*, 2021, **865**, 158926.
58 K. Kwatek and J. L. Nowiński, *Solid State Ionics*, 2018, **322**, 93–99.
59 C. Wang, Z.-G. Liu, P.-P. Lin, X. Xu, F.-G. Lu, J.-J. Xu, Y.-H. Shi, P. He and T.-S. Lin, *J. Eur. Ceram. Soc.*, 2022, **42**, 2290–2298.
60 P. Dong, Q. Jiao, Z. Zhang, M. Jiang, C. Lin, X. Zhang, H. Ma, B. Ma, S. Dai and T. Xu, *J. Am. Ceram. Soc.*, 2022, **105**, 3252–3260.
61 G. Bieker, M. Winter and P. Bieker, *Phys. Chem. Chem. Phys.*, 2015, **17**, 8670–8679.

62 S. He, Y. Xu, Y. Chen and X. Ma, *J. Mater. Chem. A*, 2020, **8**, 12594–12602.
63 H. Wang, G. Zhao, S. Wang, D. Liu, Z. Mei, Q. An, J. Jiang and H. Guo, *Nanoscale*, 2022, **14**, 823–832.
64 X. Miao, H. Di, X. Ge, D. Zhao, P. Wang, R. Wang, C. Wang and L. Yin, *Energy Storage Mater.*, 2020, **30**, 170–178.
65 Z. X. Huang, X. L. Zhang, X. X. Zhao, Y. Y. Zhao, V. Aravindan, Y. H. Liu, H. Geng and X. L. Wu, *Inorg. Chem. Front.*, 2022, **10**, 37–48.
66 C. Zhenjie, M. Yayun, D. Qingyu, J. Feng, S. Yanbin and C. Liwei, *Acta Phys.-Chim. Sin.*, 2019, **35**, 868–875.
67 J. J. Fan, P. Dai, C. G. Shi, Y. Wen, C. X. Luo, J. Yang, C. Song, L. Huang and S. G. Sun, *Adv. Funct. Mater.*, 2021, **31**, 2010500.
68 X. He, P. Ping, D. Kong, G. Wang and D. Wang, *Int. J. Energy Res.*, 2022, **46**, 23173–23194.
69 Z. Jian, W. Han, X. Lu, H. Yang, Y. S. Hu, J. Zhou, Z. Zhou, J. Li, W. Chen, D. Chen and L. Chen, *Adv. Energy Mater.*, 2013, **3**, 156–160.
70 M. K. Sadan, H. Kim, C. Kim, S. H. Cha, K. K. Cho, K. W. Kim, J. H. Ahn and H. J. Ahn, *J. Mater. Chem. A*, 2020, **8**, 9843–9849.
71 X. Liu, X. Jiang, F. Zhong, X. Feng, W. Chen, X. Ai, H. Yang and Y. Cao, *ACS Appl. Mater. Interfaces*, 2019, **11**, 27833–27838.
72 F. He, J. Kang, T. Liu, H. Deng, B. Zhong, Y. Sun, Z. Wu and X. Guo, *Ind. Eng. Chem. Res.*, 2023, **62**, 3444–3464.
73 H. Gao, L. Xue, S. Xin, K. Park and J. B. Goodenough, *Angew. Chem., Int. Ed.*, 2017, **56**, 5541–5545.
74 J.-J. Kim, K. Yoon, I. Park and K. Kang, *Small Methods*, 2017, **1**, 1700219.